Physics of Fluids

# Air flow quality analysis of an open-circuit boundary layer wind tunnel and comparison with a closed-circuit wind tunnel

Cite as: Phys. Fluids **32**, 125120 (2020); https://doi.org/10.1063/5.0031613
Submitted: 04 October 2020 . Accepted: 28 November 2020 . Published Online: 28 December 2020

María Jiménez-Portaz, Luca Chiapponi, María Clavero, and Miguel A. Losada

View Online Export Citation CrossMark

ARTICLES YOU MAY BE INTERESTED IN

A comparative study of quasi-stable sheet cavities at different stages based on fast synchrotron x-ray imaging
Physics of Fluids **32**, 123316 (2020); https://doi.org/10.1063/5.0031433

Extension at the downstream end of turbulent band in channel flow
Physics of Fluids **32**, 121703 (2020); https://doi.org/10.1063/5.0032272

Turbulent flow and heat flux analysis from validated large eddy simulations of flow past a heated cylinder in the near wake region
Physics of Fluids **32**, 125119 (2020); https://doi.org/10.1063/5.0031831


AIP Publishing



© 2020 Author(s).

Physics of Fluids ARTICLE scitation.org/journal/phf

# Air flow quality analysis of an open-circuit boundary layer wind tunnel and comparison with a closed-circuit wind tunnel

Cite as: Phys. Fluids 32, 125120 (2020); doi: 10.1063/5.0031613
Submitted: 4 October 2020 • Accepted: 28 November 2020 •
Published Online: 28 December 2020

View Online Export Citation CrossMark

María Jiménez-Portaz,[1,a)] Luca Chiapponi,[2] María Clavero,[1] and Miguel A. Losada[1]

## AFFILIATIONS

[1]Instituto Interuniversitario de Investigación del Sistema Tierra en Andalucía, Universidad de Granada, Avda. del Mediterráneo, s/n, 18006 Granada, Spain

[2]Dipartimento di Ingegneria e Architettura (DIA), Università di Parma, Parco Area delle Scienze, 181/A, 43124 Parma, Italy

[a)]**Author to whom correspondence should be addressed:** mjportaz@ugr.es

## ABSTRACT

The wide use of wind tunnels, as a tool to measure the flow properties and the flow effects on different structures/ecosystems, makes it necessary to guarantee the correct functioning of the facility and to carry out a continuous monitoring. The aim of this work is (i) to check the homogeneity and quality of the air flow in an open-circuit boundary layer wind tunnel, (ii) to provide data and ideas that could help other researchers to improve similar tunnels, and (iii) to compare some of the results with the behavior of a classic closed-circuit wind tunnel. Experiments are carried out working with a constant reference velocity, using a hot cross wire anemometry system to obtain high resolution measurements, in the entrance and test sections for different longitudinal and cross planes. The results concern the characteristics of the mean and turbulent flow. In this manuscript, we report the analysis of the turbulence production, the Reynolds stresses, the vertical velocity skewness, the vorticity, and the spectral properties, and a quadrant decomposition is also performed. Finally, comparing the results with respect to a closed-circuit wind tunnel, it is shown that the turbulence intensity is generally higher and the mean flow is more homogeneous in the present open-circuit wind tunnel. Moreover, the Reynolds number is similar in both tunnels, which indicates that both tunnels are mechanically similar.

*Published under license by AIP Publishing.* https://doi.org/10.1063/5.0031613

## I. INTRODUCTION

The multidisciplinary interest and the recent increase in the use of wind tunnels are an expression of the need to study the flow field and the effects of turbulence in a wide variety of practical cases. A classical example is the study of a model aerodynamics, or the characterization of the Atmospheric Boundary Layer (ABL), whose kinematic properties are fundamental to quantify the impact of wind on infrastructures.[1] In addition, in recent years, there has been an increasing interest in the study of the flow around renewable energy systems,[2] around forests or different types of vegetation, and around ecosystems. Furthermore, in a wind tunnel, it is also possible to study (i) the dispersion processes of pollutants, dust and pollen, and (ii) the evolution of parameters such as the Reynolds number in the presence of obstacles such as a group of trees and/or buildings.[3,4]

Based on the shape, wind tunnels are classified into two main types: open-circuit wind tunnel and closed-circuit wind tunnel. In an open-circuit tunnel, the air flow follows a straight path from the entrance through a contraction zone to the test section, followed by a diffuser, a fan section, and an outlet. Such a tunnel may have a test section with no solid boundaries (Eiffel type) or solid boundaries (NPL type, which stands for National Physical Laboratory type). On the contrary, in a closed-circuit wind tunnel, the air recirculates continuously with little or no exchanges with the outside. A closed-circuit tunnel with no solid boundaries at the test section is called Prandtl tunnel, whereas it is defined as Göttingen tunnel if solid boundaries are present at that section. Nevertheless, it should be


Published under license by AIP Publishing

remembered that almost endless variations on the specific features of the various tunnels are possible.[5]

Open-circuit wind tunnels have the advantage of being more economical and easier to build than closed-circuit tunnels. However, the open-circuit type is influenced by atmospheric conditions, with a strong dependence on (i) the architecture of the room in which the tunnel is located, (ii) the size and shape of the different parts of the tunnel, and (iii) the type of material used to construct the tunnel, mainly wood, so the structure could expand or contract with the weather and be affected by humidity.[5] In addition, continuous monitoring is necessary to ensure the homogeneity and quality of the flow, and a strict testing protocol must be followed to prevent any exchange with adjacent rooms, even avoiding the occasional entry of air through doors and windows. Closed-circuit tunnels allow a better control of the flow, which is independent from the outer conditions, and they are usually less noisy than open-circuit tunnels.

A boundary layer wind tunnel offers the possibility to measure both the flow properties and the flow effects on different structures. The wind is initially characterized by parallel current lines and a constant mean velocity, and then, it evolves depending on the surface roughness elements that are strategically arranged for the generation of the desired ABL.[5] In general, the aim of an experimental study in a wind tunnel is to obtain the mean and instantaneous values of the kinematic variables of the air flow, and in some cases, the forces, pressures, and moments that wind exerts on the scaled structures.

For the characterization and analysis of the ABL evolution in a wind tunnel, a sufficiently large and homogeneous section is needed, with a tunnel length approximately eight to ten times the height of the section.[6] Such a length guarantees the homogeneity of the flow at the test section, and it is necessary to have enough space for placing the energy dissipating devices designed to model the target ABL. The precise definition of all the geophysical variables that affect the ABL over complex areas is non-trivial matter, and it is essential to reproduce the physical characteristics of wind flow and its interaction with the scaled models. The control of all these variables and the fulfillment of the similarity conditions allow for the extrapolation of the results to reality.[7]

Wind tunnel tests provide a large amount of information and data, which represent a fundamental support to decision making for the management and planning of projects.[8] Currently, in order to obtain more accurate and reliable results, data are frequently validated and compared with *in situ* measurements[9] and numerical simulations. For example, Computational Fluid Dynamics (CFD) methodologies were used to improve the ABL generation and to design an optimized setup for an open-jet facility.[10] Comparative studies between tunnel tests and numerical simulations were also useful for a proper and optimal design of new tunnels.[8]

The aim of this study is (i) to describe the average and turbulent flow in an open-circuit boundary layer wind tunnel, (ii) to compare the performances with those of a closed-circuit wind tunnel, which has a similar geometry of the test section and to analyze the differences between them, and (iii) to highlight critical issues that may be common to tunnels of the same type, providing data and ideas useful for the management and the improvement of these facilities. This paper presents detailed analysis that are not available in the literature, especially for a tunnel located in a hosting room, which was not designed for that purpose. Present results can serve as a reference and recommendation for the construction and testing of future wind tunnels.

To the best of our knowledge, there is no direct comparison between data taken in an open circuit wind tunnel (OCWT) and the same measurements in a closed circuit wind tunnel (CCWT), with similar geometry, almost equal test section dimensions, and using the same type of instrument for data recording.

We have studied the flow characteristics in both the transversal and longitudinal planes, as well as the effects generated by the walls and the floor. An exhaustive knowledge of the mechanical behavior of the facility is required to plan improvements of the present tunnel, even considering a possible transformation in a climatic tunnel, with the ability to control variations in temperature, humidity, etc. Recently, many works have included climatic conditioning to classical studies conducted in wind tunnels.[11–13] Therefore, this paper is a research activity that is necessary for the development of such additional and relevant features, and that could help other researchers willing to do the same.

This paper is organized as follows: in Sec. II, fundamentals of the use of the wind tunnels, experimental setup, physical quantities, and scales used in this work are detailed. The main results are presented and discussed in Sec. III, including the analysis of the turbulence production, the Reynolds stresses, the vertical velocity skewness, the vorticity and the spectral properties, and a quadrant decomposition of the turbulence structure. The comparison between the present tunnel and a CCWT tunnel is analyzed in Sec. IV, and finally, the main conclusions are summarized in Sec. V.

## II. STUDY CASE AND METHODOLOGY

In 2004, a boundary layer wind tunnel was built in the Laboratory of Environmental Hydraulics at the Andalusian Institute for Earth System Research (IISTA, University of Granada).

The IISTA wind tunnel is an open-circuit facility and its total length is equal to 22 m. The closed test section is 13.6 m long, with a 2.15 m wide and 1.80 m high cross section, constant in the longitudinal direction. Therefore, the tunnel layout is of the NPL type. The choice of an open-circuit design was due, among other reasons, to space limitations. Figure 1(a) shows the arrangement of the tunnel inside the laboratory. The schematic view and more technical details can be found in Figs. 1(b) and 1(c). The flow velocity can be regulated from 1 m/s to 55 m/s.

In the past years, the tunnel has been used for many research activities, also involving the interaction between the wind field and ecosystems and the aerodynamic effects on infrastructures and its interaction with the environment.[14–17]

### A. Experimental setup

Systematic measurements of the wind velocity were taken working with a constant reference velocity, which was obtained setting the rotation rate of the turbine. In the case of the IISTA tunnel, the rotation generates a suction effect, which is responsible for the air entering by the inlet and flowing through the test section toward the turbine and the outlet. The operation of the device induces an unavoidable air recirculation inside the room housing the tunnel [Fig. 1(a)].


Published under license by AIP Publishing

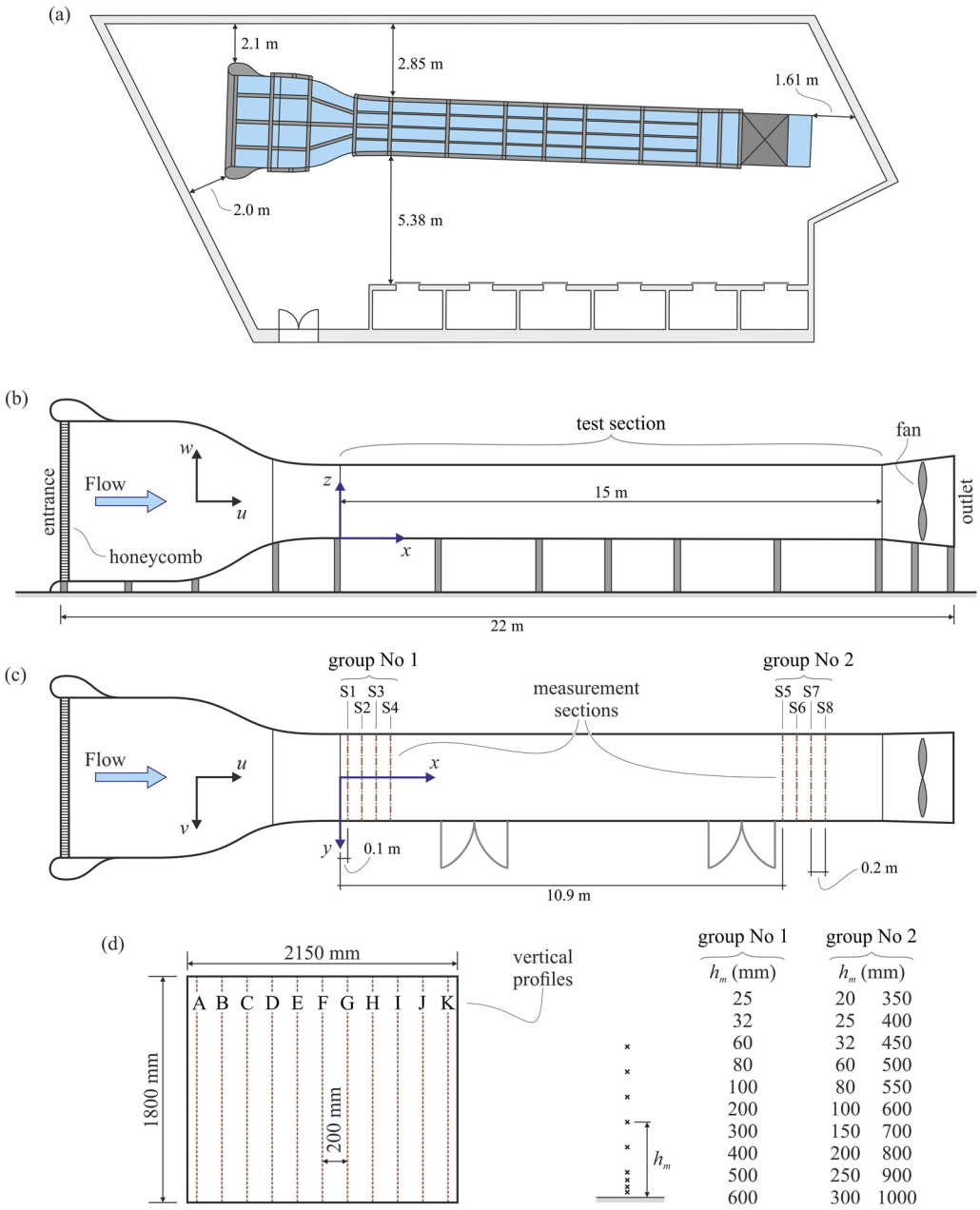


**FIG. 1**. Experimental setup. (a) Sketch of the wind tunnel inside the IISTA laboratory. (b) Front view. (c) Top view with details of the sections where the measurements have been taken. (d) Layout of the vertical profiles (A–K) in the cross section; $h_m$ is the distance from the bottom of the points where the speed has been measured.

A TSI constant temperature anemometer was used to obtain high-resolution and instantaneous measurements of the streamwise and vertical velocity components, $u$ and $w$ respectively. A cross-wire X-probe (model 1241 − 20) was controlled by the IFA-300 board. The hot wire is held by a TSI Standard Probe Support which in turn is connected to a 3D positioning system. This positioning system is rigid, and it is fixed with screws onto the surface of the tunnel avoiding any possible vibration. The probe has a total length of 47.5 mm including the hot wire, and the sensor diameter is equal to 3.2 mm. The probe was placed perpendicular to the air flow, with the wires oriented so as to obtain the longitudinal component and the vertical component of the wind speed vector.

The principle of operation of this instrument is based on the heat transfer from the sensor to the surrounding fluid medium. The


Published under license by AIP Publishing

**TABLE I**. Tests carried out for each section and characteristics of data measuring and reference values.

| | Entrance section | Tests section |
|---|---|---|
| No. of vertical profiles | 44 | 44 |
| No. of points per profile | 10 | 20 |
| No. of total wind time series | 440 | 880 |
| Wind reference velocity (m/s) | 3, 7.5, 10 | 3, 7.5, 10 |
| Sample frequency (Hz) | 1000 | 1000 |
| Duration of the test (s) | 130 | 130 |

relation between the sensor voltage output and the flow velocity is established by means of a calibration transfer function. The IFA 300 system is characterized by a frequency response up to 300 kHz, depending on the sensor used. The high-pass filter was disabled and the low-pass filter was set to 1 kHz. During the calibration process a thermocouple system is used to reduce uncertainty and incorporate temperature variations. The average absolute difference between the instrument readings and the actual values (i.e., the velocities imposed during calibration) is of the order of 2 mm/s; this gives an estimate of the instrumental accuracy. The measurements in some points were also repeated on different days, in order to check the reproducibility of the experiment.

Eight different cross sections were selected for the data acquisition, four at the entrance of the test section (group No 1, starting at $x = 0$ m) and four at its end (group No 2, starting at $x = 10.9$ m); see Fig. 1(c). Considering one group at a time, the cross sections are 0.20 m apart from each other for group No 1, and 0.175 m for group No 2, and 11 equally spaced vertical profiles were acquired in each of them. The vertical resolution in group No 2 is finer to give a better description of the flow field in the testing region, where physical models are located for research activities and the boundary layer is more developed.

Figure 1(d) shows the position of the profiles within a section. The velocity was measured in several points along each vertical profile; ten points in the case of profiles belonging to group No 1 and 20 points for group No 2. In sum, a total of 1320 wind speed time series were acquired for a given wind reference velocity. All these data are summarized in Table I. The spacing of the points on the vertical increases from the bottom to the top, as the influence of the tunnel surface decreases. The 3D positioning system allows the probe to be accurately placed in the desired position.

Since spectral and turbulence analysis require a high sampling rate, data were acquired at each point with a sample frequency of 1 kHz for at least 130 s, under ergodicity assumption. A first statistical elaboration of the temporal series is necessary to perform a real-time monitoring of the acquisitions. An example of the time series obtained is shown in Fig. 2, for the two sections and three representative heights. At a height of 0.025 m there is a strong influence of the wind tunnel surface. The low frequency content is related to the presence of coherent structures that are generated close to the bottom. Hairpin-like vortices[18] may follow each other, growing outwards from the wall and being responsible for this experimental evidence.

This analysis and data recording were performed using Thermal Pro software®. Measurements were repeated with three different reference wind velocities (see Table I), which fall in the range most commonly used in the study of environmental systems.

## B. Physical quantities and scales

Experimental results from this work are reported as mean and turbulent characteristics of the flow in the entrance and test sections of the tunnel. $\langle u(z) \rangle$ is the mean streamwise velocity at a height equal to $z$. As a velocity scale, we adopted the reference velocity (7.5 m/s).

The Reynolds number is defined as

$$Re = \frac{\rho \langle u \rangle D_t}{\mu}, \tag{1}$$

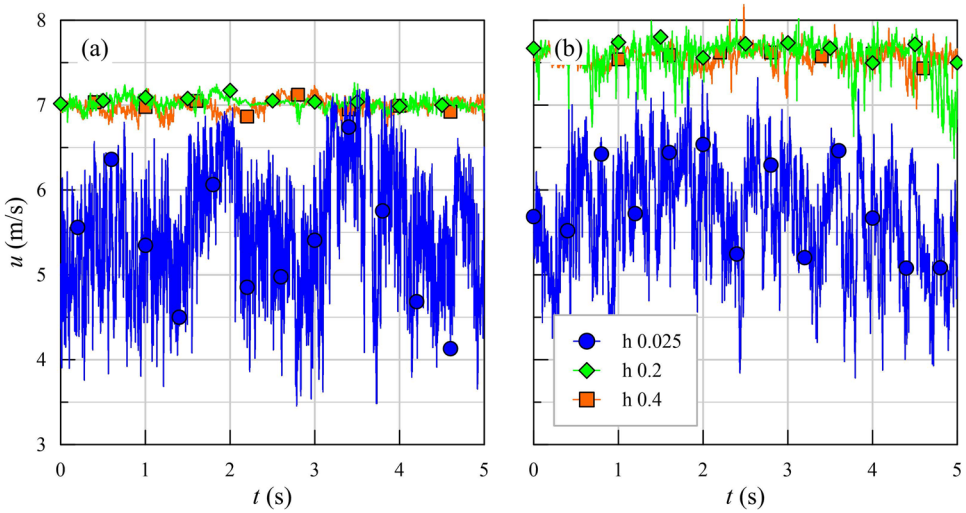


**FIG. 2**. Time series recorded for (a) entrance section (S1) and (b) tests section (S5) for three representative heights.


Published under license by AIP Publishing

where $\mu$ is the dynamic viscosity of the air, $\rho$ is the air density, and $D_t = 1.96$ m is the hydraulic diameter of the wind tunnel defined as

$$D_t = \frac{2ab}{a+b}, \tag{2}$$

where $a = 1.8$ m and $b = 2.15$ m are the height and the width of the tunnel section, respectively.

Notice that the velocity range of the present experiments ensures the flow is fully turbulent ($Re = 1.05 \cdot 10^6$) and the viscosity effects on a local scale are minimal. This condition (i) is satisfied when the Reynolds number is greater than 2300 (critical $Re$ for the pipe flow) and (ii) must be guaranteed in the case of tests performed on reduced scale model in order to have a mechanically similar flow around the model and the prototype.[19,20]

The turbulent part, or wind fluctuations $u'$, is defined as the instantaneous value of the wind speed minus the mean value; such a definition can be applied to all the other variables of interest.[21] Therefore, the variance $\sigma^2$ is defined as

$$\sigma_u^2 = \overline{u'^2}, \qquad \sigma_w^2 = \overline{w'^2}. \tag{3}$$

The turbulence intensity, as the simplest descriptor of the atmospheric turbulence for the $x$ direction, is defined as $IT$ and derived from the variance,

$$IT(z) = \frac{\sigma_u(z)}{U(z)}. \tag{4}$$

Moreover, to obtain the kinematic momentum flux, the following expression was used:[21]

$$u_*^2 = |\,\tau/\rho\,| = |\,\overline{u'w'}\,|, \tag{5}$$

where $u_*$ is the friction velocity, $\tau$ is the Reynolds stress, and $\rho$ is the air density.

The velocity fluctuations of the wind are caused by the superposition of eddies, which are transported by the mean flow. Turbulence is characterized by vorticity and energy transfer processes, and it can be analyzed and represented through its energy spectrum, among others variables.

The energy spectrum can be obtained using the Fourier transform of its auto-correlation function. From the energy spectral density function, it is also possible to represent how the Turbulent Kinetic Energy ($TKE$) is distributed with respect to the frequency.[22]

There is a relationship between the generation of turbulent Reynolds stresses and the interaction between vorticity and the velocity field. The vorticity, which is twice the rate of rotation of the fluid,[23] is also defined as the curl angular velocity (CAV),

$$\mathrm{CAV} = \nabla \times \mathrm{u}. \tag{6}$$

A positive angular velocity indicates a counter-clockwise rotation. In the present work, the vorticity has been calculated only in longitudinal planes, since just two components of the wind velocity are available (longitudinal, $x$, and vertical, $z$).

## III. RESULTS AND DISCUSSION

The present section describes the results of measurements and data processing, with the aim of characterizing the flow field in the entrance and test regions. The area of the cross section where the flow can be tested without being affected by the blockage effect is defined, and this will be useful for planning the future research activities.

### A. The mean flow

To check the characteristics of the flow field and validate the wind tunnel in the present configuration, the average values of the velocity are analyzed at first. Figure 3 shows the contour of the dimensionless wind velocity, $u/u_{ref}$, for all the investigated sections (both in the entrance and in the test regions), with the effect of the

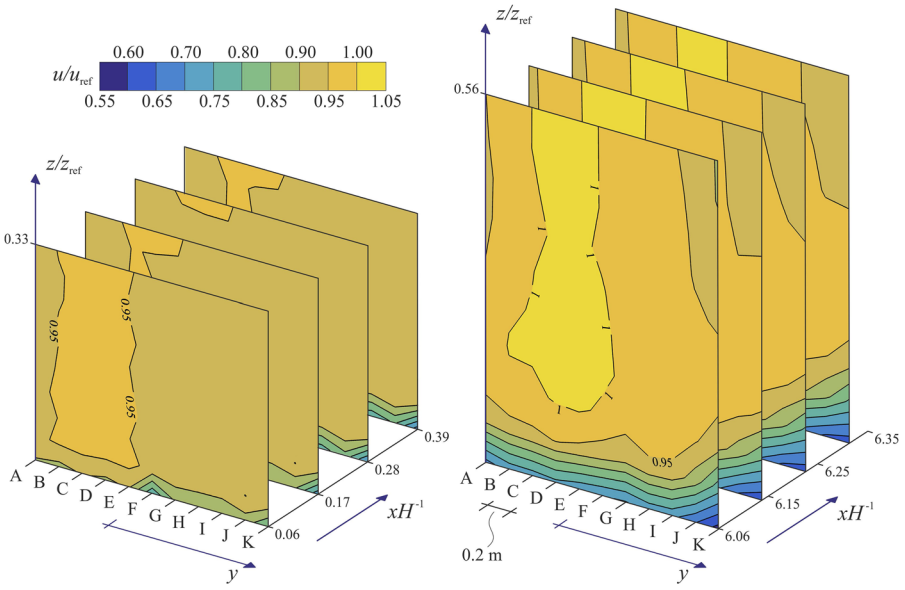


**FIG. 3**. Mean streamwise velocity of the wind, $u/u_{ref}$, in the entrance region (a) and in the test region (b). The color bar is the same for both panels.


Published under license by AIP Publishing

solid boundaries: flow retardation and turbulence enhancement in the areas adjacent to the walls. However, it is possible to observe that, outside the boundary layer and at a sufficiently large distance from the side walls, the homogeneity of the wind field is fairly good. Few vertical patterns are visible and they may be due to an asymmetry in the flow resistances outside and/or inside the tunnel. The different spacing of the walls surrounding the tunnel could prevent an uniform air supply at the entrance. Moreover, some imperfections on the side walls (e.g., very small steps between the covering panels) may arise as a consequence of the thermal deformations of the structure, and they could be responsible for local variations in roughness.

The mean velocity profiles in the near-wall region of a turbulent boundary layer over rough walls can be expressed by the logarithmic profile. This gives the velocity at a height above the surface $u(z)$ as

$$u(z) = \frac{u_*}{k} \ln(z/z_0), \tag{7}$$

where $z_0$ is the aerodynamic roughness length, $u_*$ is the friction velocity, and $k$ is the von Karman constant, taken here as 0.41. In the present study, a logarithmic profile is evident in the test region, where the data fitting allows us to obtain both the values of $z_0$ and $u_*$. On the contrary, the wind profile at the entrance is not sufficiently developed and there are not enough measurements near the bottom to carry out any quantitative evaluation. The roughness length is almost constant in the test region and it is of the order of $1 \times 10^{-4}$ m, with very limited variations except near the right wall (for $y = 1$ m). Figure 4(a) shows some of the measured profiles in the test region and the thickness, $z_b$, of the boundary layer. The value $z_b = 0.18$ m, obtained by means of the classical 99% method, is in accordance with the values 0.181 and 0.188 calculated using the well-known expression[24]

$$z_b = 0.37 \frac{x}{\mathrm{Re}_x^{1/5}} \tag{8}$$

for sections S5 and S8, respectively. $\mathrm{Re}_x = ux/\nu$ is the Reynolds number in the $x$ direction, and $\nu$ is the kinematic viscosity of the air.

The friction velocity map in the test region is represented in Fig. 4(b), and it is possible to observe that $u_*$ is almost constant, with most of the values in the range 0.38 m/s–0.40 m/s. Again, near the right wall, an anomaly is present with the friction velocity decreasing to 0.2 m/s. This behavior can be due to the asymmetry of the hosting room or to a local disturbance (e.g., a discontinuity in the bottom coating).

A comparison of some velocity profiles with the classical law of the wall is shown in Fig. 5(a). In the logarithmic region,

$$u^+ = \frac{1}{k} \ln(y^+) + C - \Delta u^+, \tag{9}$$

where $u^+ = u/u_*$ and $y^+ = zu_*/\nu$ are dimensionless velocity, $C$ is assumed to be a constant for smooth-walled flows ($C = 5.1$ according to Ref. 19), and $\Delta u^+$ is defined as the roughness function and it represents a roughness-caused shift. As expected for a rough surface, the experimental profiles are located below the smooth wall profile, with $\Delta u^+ \approx 8.5$.

Near a rough wall, the characteristic scale instead of being controlled by a frictional scale may be controlled by roughness length $z_0$; if $z_0 > z_f \equiv \nu/u_*$, a better scaling is $z^+ = z/z_0$, as shown in Fig. 5(b).

A summary of the main parameters and variables that define the boundary layer obtained for the tests section is shown in Table II.

## B. Spectral analysis

The energy distribution in the frequency domain is described by the power spectrum, which has a significant influence (i) on the wind–structure interaction and (ii) on the aerodynamic loads.[25]

In particular, turbulence has a wide range of length (time) scales. As is known, the fluctuation energy is produced at the large eddies (with low frequencies). The vortex stretching mechanism then generates smaller and smaller eddies, and energy flows down the spectrum to high frequency region. Finally, the energy is mainly dissipated into heat at the smallest eddies (of the order of the Kolmogorov scales). Larger eddies have a significant contribution to the aerodynamic loads; however, smaller eddies can affect bluff bodies more.[25] Inside the boundary layer, the turbulent eddies

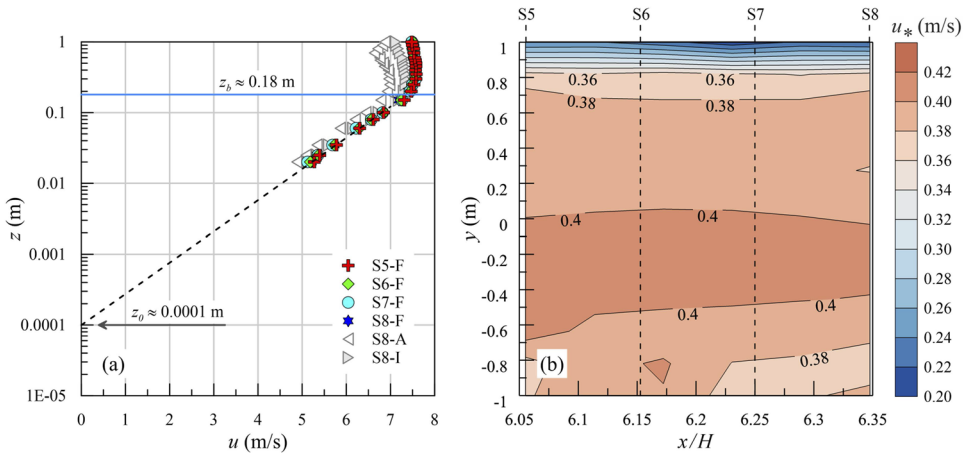


**FIG. 4.** Vertical profiles of the mean wind velocity (a) and friction velocity map (b) in the test region. $z_0$ is the roughness length and $z_b$ is the boundary layer length. For clarity, only a limited number of profiles are shown in panel (a).


Published under license by AIP Publishing

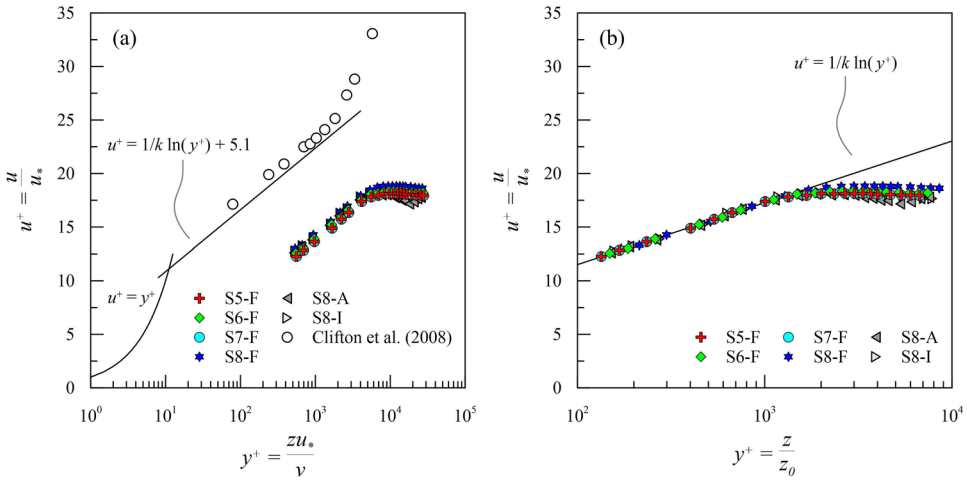


**FIG. 5**. Vertical profiles of wind speed and turbulence intensity measured in the tunnel entrance section (a) and in the tunnel test section (b).

transfer momentum deficit away from the surface, meaning that a low momentum fluid is transported away from the surface and replaced by fluid with more momentum that came from above the surface.

The power spectra of the streamwise velocities are calculated via FFT (Fast Fourier Transform) and compared with the classical von Karman formula[26] for the dimensionless spectrum of the longitudinal component of atmospheric turbulence,

$$\frac{nS_u(n)}{\sigma_u^2} = \frac{4n_u}{(1+70.8n_u^2)^{5/6}}, \tag{10}$$

where $n_u = nL_u/U$, $n$ is the frequency, $U$ is the longitudinal mean wind speed, $\sigma_u$ is the standard deviation, and $L_u$ is the longitudinal length scale. It is proved (for large $n$) that if a von Karman spectrum is plotted on log–log axes, the high frequency part of the spectrum will approximate to a straight line of gradient −5/3. The position of this line is determined by $U$, $\sigma_u$, and $L_u$.

Figure 6 shows two spectra obtained at heights $z = 0.08$ m and 1.00 m in the test region (section S8, profile F). Values of the spectral function decrease as the distance from the tunnel floor $z$ is increased. It is also possible to see a good definition of the inertial subrange (−5/3 slope) starting at a frequency ≈10 Hz.

The comparison with Eq. (10) was obtained for the spectra measured at different heights and in different sections, but it is only shown for the spectra represented in Fig. 6. The agreement is fairly good both in and out of the boundary layer.

**TABLE II**. Boundary layer characteristics: average value in sections S5–S8.

| Section | $z_b$ | $z_0$ (m) | $u_*$ (m/s) |
|---|---|---|---|
| S5 | 0.181 | $0.99 \cdot 10^{-4}$ | 0.382 |
| S6 | 0.183 | $1.09 \cdot 10^{-4}$ | 0.382 |
| S7 | 0.186 | $1.02 \cdot 10^{-4}$ | 0.373 |
| S8 | 0.188 | $0.96 \cdot 10^{-4}$ | 0.371 |

## C. Vorticity

The vorticity describes the local spinning motion of a continuum (e.g., the tendency of the fluid to rotate), and it is twice the local rotation rate. The curl angular velocity (CAV) is shown in Fig. 7 for two longitudinal sections in the inlet region [panels (a) and (b)] and for two longitudinal sections in the test region [panels (c) and (d)]. It is possible to observe that the CAV is almost nil out of the boundary layers, while it increases toward the bottom up to −20 $s^{-1}$ in the test region and up to −60 $s^{-1}$ in the entrance region. The minus sign indicates a clockwise rotation direction. The generation of vorticity in the inlet region can be attributed to some small irregularities

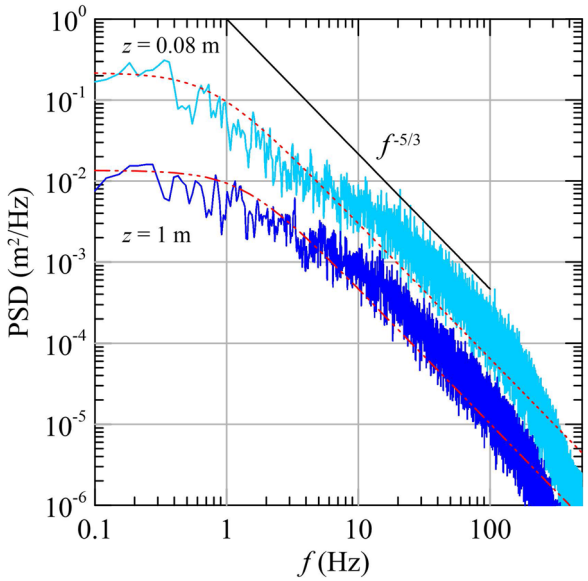


**FIG. 6**. Power spectral density of the streamwise velocity in section S8 (test region) at different heights. Dashed and dotted-dashed lines are the von Karman spectra.


Published under license by AIP Publishing

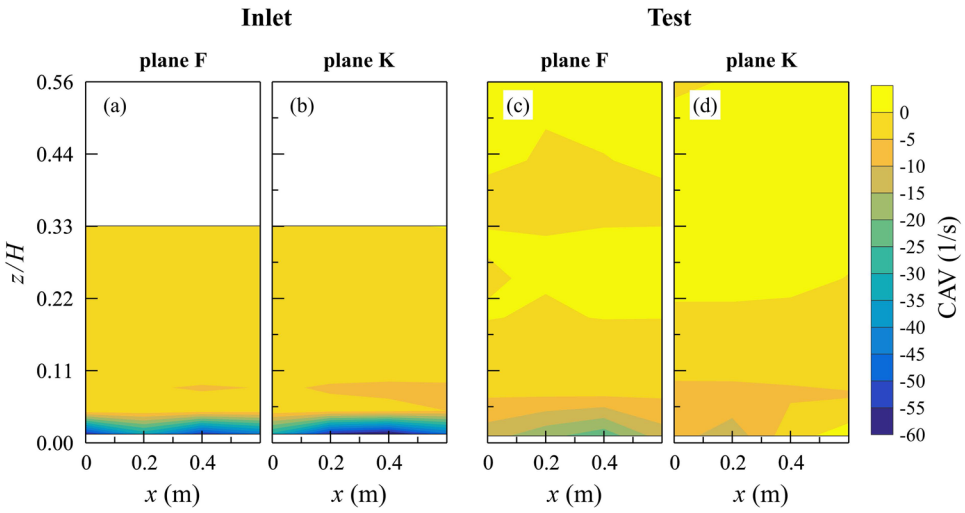


**FIG. 7**. Curl angular velocity map. Inlet region: (a) plane F and (b) plane K. Test region: (c) plane F and (d) plane K.

between the section S1 and the entrance of the tunnel. No appreciable variation is present between planes F and K, which are at the center of the tunnel and close to the wall, respectively.

Figure 8 shows the profiles of the CAV (averaged in the $x$ and $y$ direction); error bars refer to one standard deviation. The variability is very low, except for the points close to the bottom, where horseshoe vortexes are generated. Their origin is related to the instability of the instantaneous velocity profile evolving into transverse vortices,[18] whose structure is described in the literature.[27]

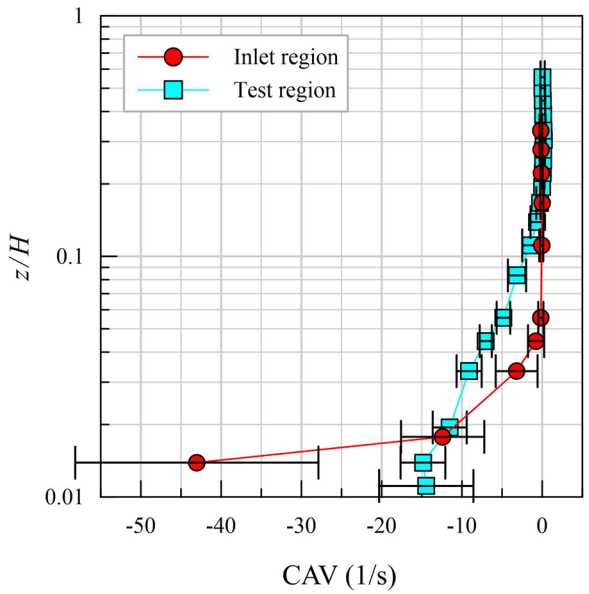


**FIG. 8**. Profiles of the CAV (averaged in the $x$ and $y$ direction) for both the inlet and the test region. Error bars refer to one standard deviation.

### D. Turbulence and Reynolds stresses

In order to study the air-flow turbulence and to provide a better characterization of the flow in both sections, the turbulence intensity (IT) in the cross sections has been analyzed.

Figures 9(a) and 9(b) show the contour map of the turbulent intensity in section S3 and section S7, respectively. It is possible to observe the influence exerted by the surface of the bottom and of the lateral walls, with the turbulent intensity presenting the maximum values inside the bottom boundary layer. The variation along the $x$ axis is practically nil within both group 1 and group 2. Most of the variables related to the turbulence are represented with a logarithmic vertical scale in order to evaluate the details in the area near the tunnel bottom due to the fact that the turbulence itself is higher right there.

Figures 9(c) and 9(d) show the vertical profiles of the turbulent kinetic energy in two sections of group 1 (S1 and S3) and in two sections of group 2 (S5 and S7), respectively. Also in this case, it is possible to observe the effect of the lateral walls with a particular asymmetry between profile A and profile K, especially in the inlet region (group 1). This behavior can be once again addressed to the positioning of the tunnel in the hosting room, with an external recirculation of the air that cannot be symmetrical.

The Reynolds shear stresses, non-dimensional with respect to the reference velocity, are shown in Fig. 10. In the inlet region, as the $x$ coordinate increases, it is possible to observe an evolution of the shear stress profile within the boundary layer. On the contrary, in the test region, there is no appreciable variation between the different sections. A layer of constant shear stress $\overline{u'w'}$ was observed in the range of $z/H = 0$ to $\approx 0.06$. Error bars refer to one standard deviation, and it is possible to observe that their maximum amplitude is reached near the bottom at the entrance and at upper limit of the boundary layer in the test region. This may be attributable to the following reasons: (i) the thickness of the boundary layer itself undergoes modest variations along the transverse direction, (ii) the side walls locally modify the entity and the distribution of shear stresses.


Published under license by AIP Publishing

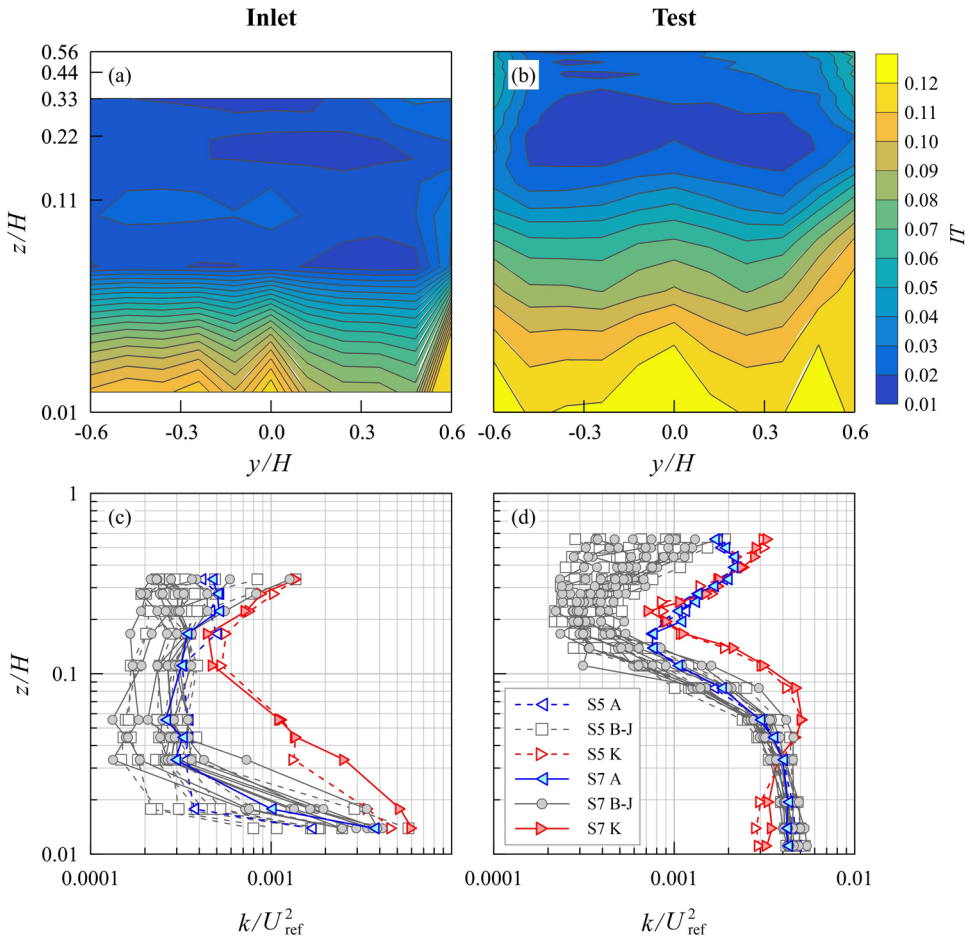


**FIG. 9**. Turbulence intensity. (a) Section S3, (b) section S7, (c) vertical profiles of the turbulent kinetic energy in section S1 (empty symbols) and S3 (filled symbols), and (d) vertical profiles of the turbulent kinetic energy in section S5 (empty symbols) and S7 (filled symbols).

### E. Reynolds stress tensor's principal axes

The interaction between the mean flow and the fluctuating velocity can also be analyzed observing the Reynolds stress tensor. In the case of the action of a constant pure plane strain on an initially isotropic turbulence,[28] the principal axes of the Reynolds stress tensor are those of the mean rate of strain, and the turbulent motion appears as oriented by the strain field. When the strain field changes, the axes of the Reynolds stress tensor have a tendency to be reoriented along the axes of the new strain, with a delay that depends on the time scale of the imposed strain. If the strain tensor reduces to a pure shear stress, for isotropic turbulence, the principal axes of the Reynolds stress tensor are not aligned with those of the strain, which is a consequence of the mean rotation. The two principal stresses in the $xz$ plane[29] are

$$\sigma_{a,b} = \frac{\overline{u'u'} + \overline{w'w'}}{2} \pm \sqrt{\left(\frac{\overline{u'u'} - \overline{w'w'}}{2}\right)^2 + \left(\overline{u'w'}\right)^2}, \quad (11)$$

and their orientation is

$$\alpha_\sigma = \frac{1}{2}\arctan\left(\frac{2\overline{u'w'}}{\overline{u'u'} - \overline{w'w'}}\right). \quad (12)$$

In the present experiments, it results in $\sigma_a/\sigma_b$ = 2–8 in the boundary layer, with the highest value close to the bottom. The ratio tends toward unity in the outer region, especially in sections S5 to S8, while its value is a bit higher in the inlet region [see Figs. 11(a) and 11(b)].

For comparison, the ranges of values in three traditional flows are

$$\sigma_a/\sigma_b = 3 \text{ to } 4 \quad \text{(boundary layer)}, \quad (13a)$$

$$\sigma_a/\sigma_b = 3 \text{ to } 5 \quad \text{(channel)}, \quad (13b)$$

$$\sigma_a/\sigma_b = 2 \text{ to } 6 \quad \text{(plane wake)}. \quad (13c)$$

The orientation angle found in the boundary layer and channel flow is $\alpha_\sigma \approx -20°$ to $-25°$ and $\alpha_\sigma \approx 70°$–$65°$, while that in the wake is $\alpha_\sigma \approx 40°$–$50°$ and $\alpha_\sigma \approx -50°$ to $-40°$, as reported by Champagne *et al.*[29]

Figures 11(c) and 11(d) show the principal axis angle of turbulence in sections S3 and S7, respectively. In the present experiments, the Reynolds stress tensor has a principal axis at ≈−15° close to the bottom, with values that progressively grow up to ≈−35° near the


Published under license by AIP Publishing

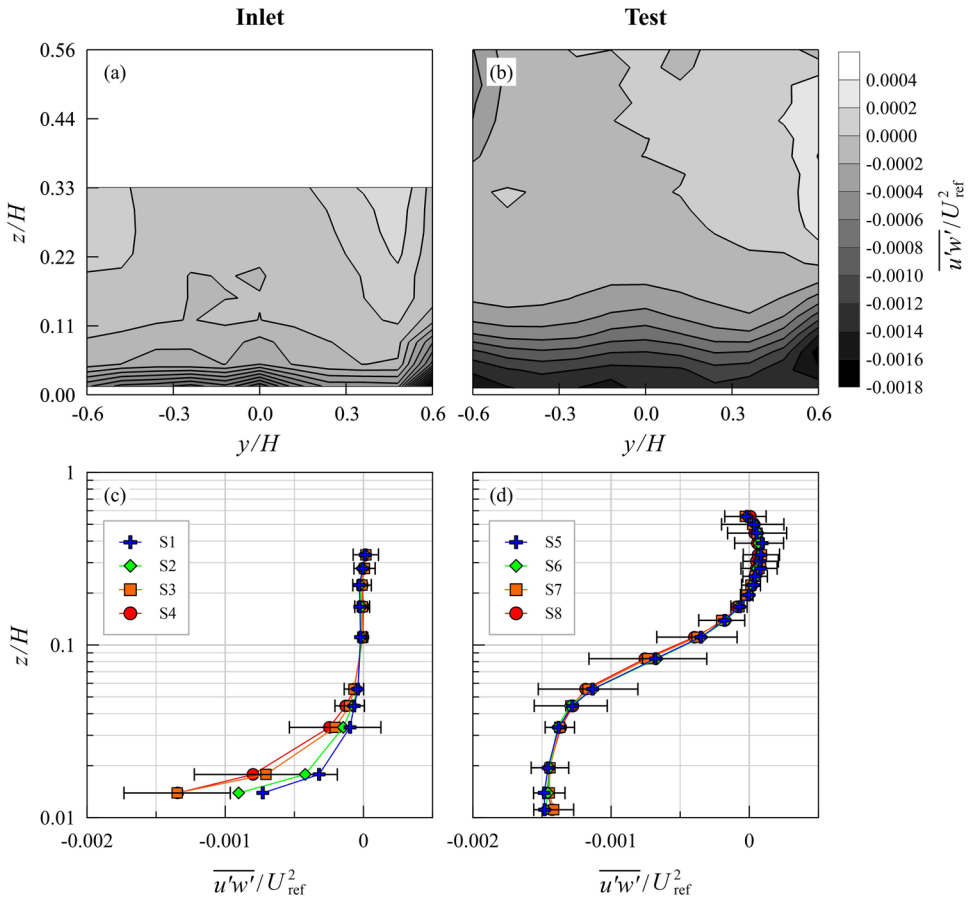


**FIG. 10**. Reynolds shear stress. (a) Section S3, (b) section S7, (c) vertical profiles averaged in the spanwise $y$ direction in the inlet region, and (d) vertical profiles averaged in the spanwise $y$ direction in the test region. Error bars refer to one standard deviation.

upper limit of the boundary layer. In section S7, it is also possible to observe the influence of the right wall where the orientation is mainly in the range ≈15° to ≈35°. In the upper part of the outer region, the pattern is not homogeneous, but we bear in mind that the values of the shear stresses are almost nil in that area, resulting in greater uncertainty in the estimation of $\alpha_\sigma$.

## F. Skewness

The statistics of turbulence can also be characterized by the vertical velocity skewness, which is given by

$$s = \overline{w'^3}/\overline{w'^2}^{3/2}, \tag{14}$$

and it is indicative of the structure of the motion,[30] since the triple correlation $\overline{w'^3}$ represents the vertical transport of $\overline{w'w'}$ by the turbulence itself. Skewness plays the same role in the equation for the evolution of turbulent kinetic energy (TKE). Hence, when $\overline{w'w'}$ (therefore skewness) is positive, both $w'w'$ and TKE are being transported upwards. That, as expected, is what happens inside the boundary layers for the present experiments. Figure 12 shows the contour map of the skewness in two different sections.

## G. Quadrant analysis

To give a more detailed description of the turbulence structure, Reynolds shear stresses contributions are categorized according to their origin and divided into four quadrants.[31] Then, conditionally sampling according to the quadrant gave the statistics of the events, as shown in Fig. 13.

The event-averaged shear stress for the $i$th quadrant is computed as

$$\langle\overline{u'w'}\rangle_i = \frac{1}{N_i}\sum_{j=1}^{N_i}\left[u'w'_j\right]_i \text{ for } i = 1,\ldots,4, \tag{15}$$

where $N_i$ is the number of events in the $i$th quadrant and $j$ is the current sample number. The average shear stress for the $i$th quadrant is

$$\overline{u'w'}_i = \frac{1}{N}\sum_{j=1}^{N_i}\left[u'w'_j\right]_i \text{ for } i = 1,\ldots,4. \tag{16}$$

The ratio, $N_i/N$, is the relative permanence of the events in the $i$-quadrant, and hence,

$$\overline{u'w'}_i = \frac{N_i}{N}\langle\overline{u'w'}\rangle_i, \tag{17}$$


Published under license by AIP Publishing

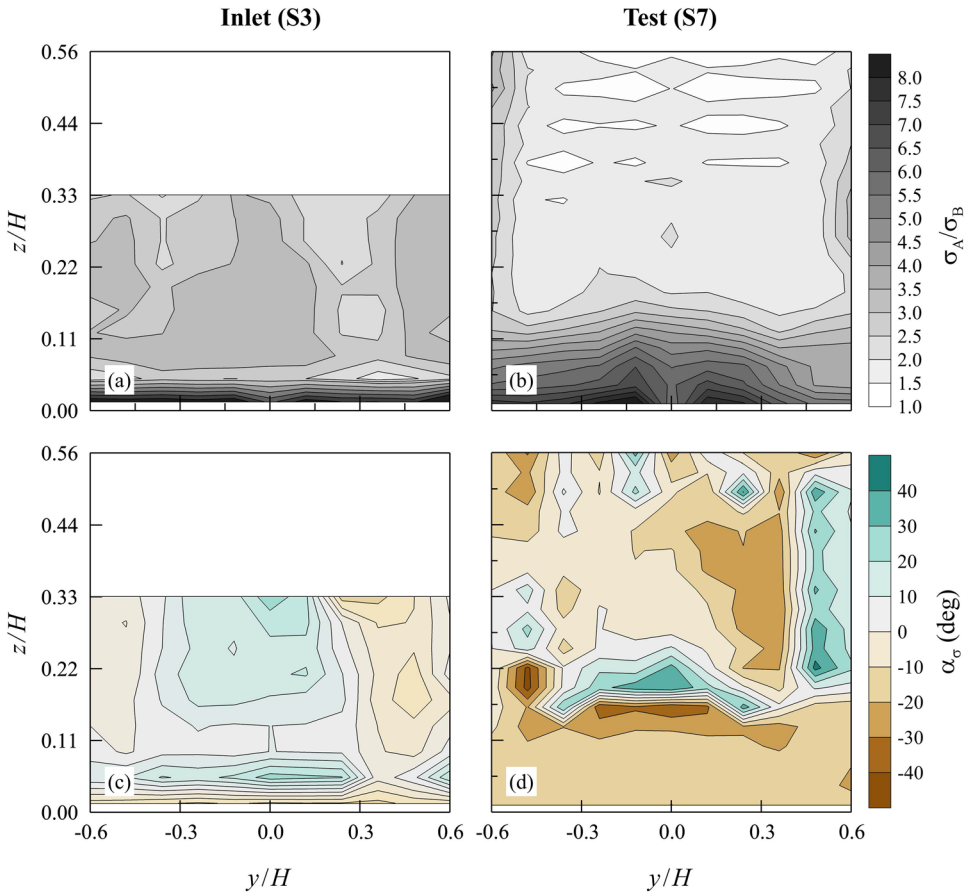


**FIG. 11**. Ratio of the maximum–minimum stresses: (a) section S3 in the inlet region and (b) section S7 in the test region. Time-averaged principal axis angle of the Reynolds stress tensor: (c) section S3 and (d) section S7.

and the total shear stress is

$$\overline{u'w'} = \sum_{i=1}^{4} \overline{u'w'}_i. \tag{18}$$

In a turbulent boundary layer, ejections and sweeps are generally the main contributors to the transfer of momentum, as it is possible to observe in Figs. 14 and 15, which show the event-averaged shear stress for the inlet and the test region, respectively.

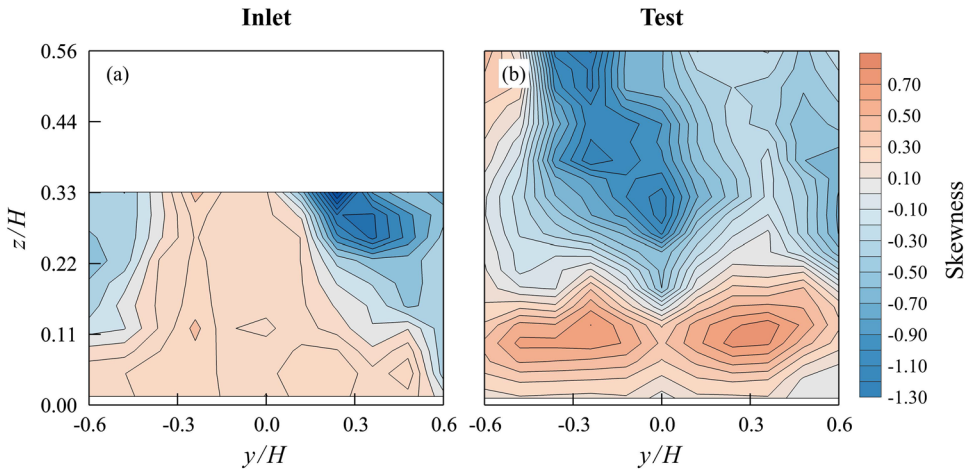


**FIG. 12**. Skewness map. (a) Section S3 in the inlet region. (b) Section S7 in the test region.


Published under license by AIP Publishing

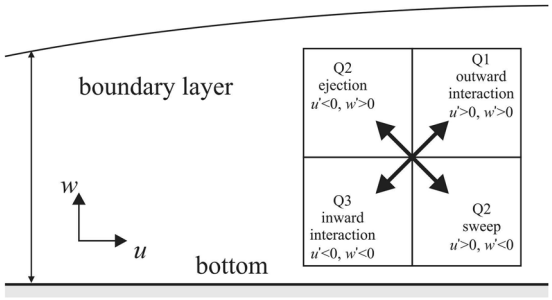


**FIG. 13**. Quadrant decomposition of the fluctuating components of the velocity.

## H. Turbulence production

The rate of energy transfer from the mean flow to turbulence is considered a production term of TKE and is given by[31]

$$P = -\overline{u'v'}\frac{\partial u}{\partial z}, \tag{19}$$

while the contribution from the $i$th quadrant is

$$P^i = -\overline{u'v'}^i\frac{\partial u}{\partial z}. \tag{20}$$

The proper scaling is through the boundary layer thickness, $\delta$, and the reference velocity, $U_{ref}$.

Figure 16 shows a contour plot of the TKE production in two different longitudinal sections belonging to the test region. In most of the tunnel (sections A–J), the energy transfer is confined to the boundary layer and reaches a maximum near the bottom.

From the quadrant decomposition, ejections appear slightly more efficient than sweeps. The inward and outward interactions (Q1 and Q3) give a negative contribution but are almost one order of magnitude smaller than the positive contribution. These results can be compared with the results from Nolan *et al.*,[32] who found dominant activity in the inner half of the boundary layer (close to the wall).

Near the right side wall (sections K), a more varied scenario is present, with peaks of production less intense and at different heights.

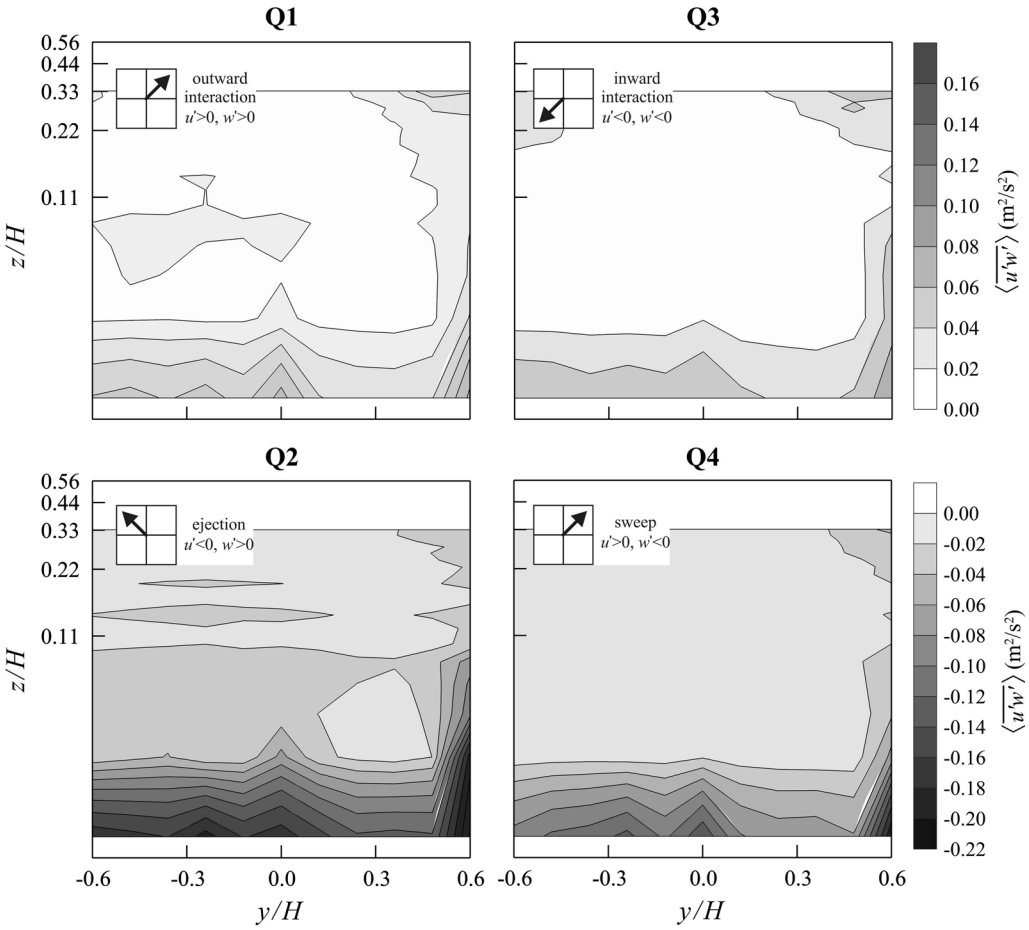


**FIG. 14**. Event-averaged shear stress quadrant decomposed for section S3 in the inlet region.


Published under license by AIP Publishing

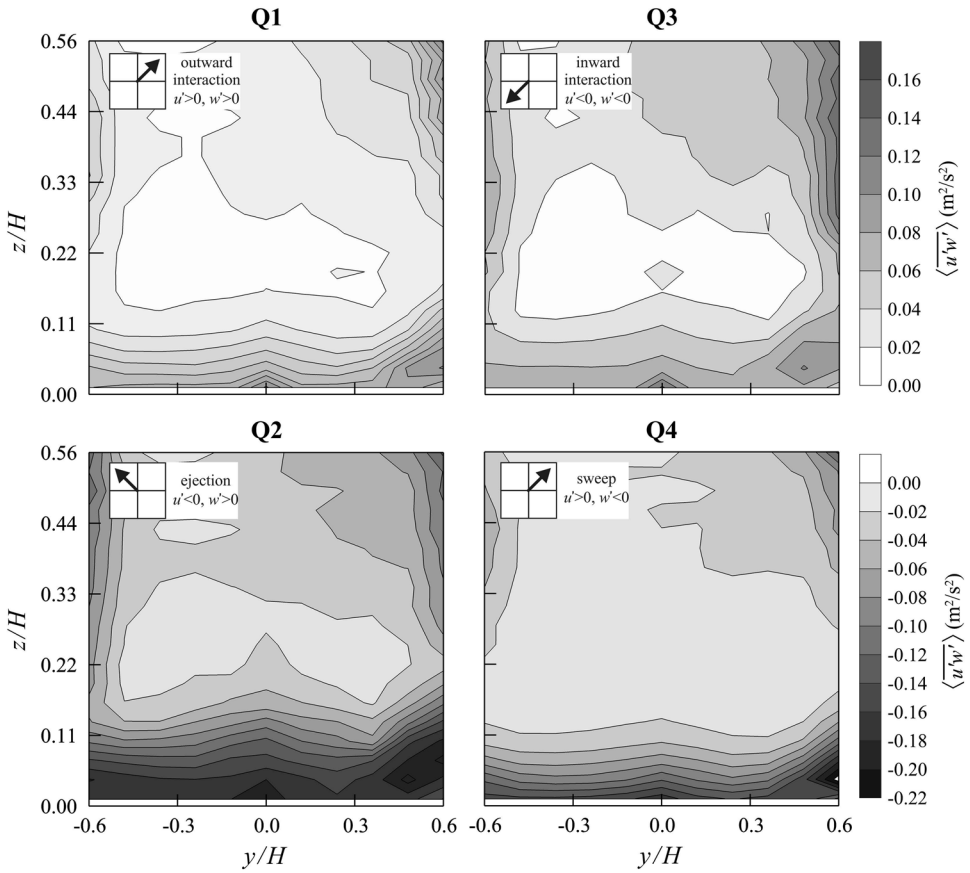


**FIG. 15**. Event-averaged shear stress quadrant decomposed for section S7 in the test region.

Figure 17 shows the distributions of the mean turbulent energy production for some vertical profiles in the test region. The distribution is similar to a self-preserving boundary layer, with minor differences near the bottom, which can be attributed to a small positive-gradient pressure in the experimental boundary layer.[31] For comparison, the zero-pressure-gradient boundary layer distribution (Klebanoff 1955) and two positive-gradient-pressure boundary layer distributions ($a = -0.15$ and $a = -0.225$), where $a$ is the exponent of the velocity variation with the fetch, $U_\infty (x - x_0)^a$, are shown. The profile K that is close to the right wall seems to be subject to a relevant positive-gradient pressure.

## IV. COMPARISON WITH A CCWT

The behavior of the IISTA wind tunnel is also compared with some literature data describing the behavior of a classic closed-circuit wind tunnel (CCWT),[13] since such a type of tunnel is generally supposed to develop a more homogeneous and uniform flow.[5]

### A. Description of the closed-circuit wind tunnel

The climatic boundary layer wind tunnel from the Center of Excellence Telč (CET) of the Institute of Theoretical and Applied Mechanics (ITAM), Prague (Czech Republic), is a Göttingen closed-circuit type wind tunnel and its layout is shown in Figs. 18(a) and 18(b). The tunnel has a 11 m long aerodynamic test section with a 1.9 m wide × 1.8 m high cross section.

The data are available in the literature and were acquired by the authors through a Dantec Dynamics cross hot-wire anemometer, with a sampling rate of 1 kHz for a period equal to 20 s at each point. The reference velocity was $u_{ref} = 13.5$ m/s. The test program and the complete description of the tests are detailed in the original manuscript.[13]

The Reynolds number has similar values in both tunnels: $Re = 1.05 \cdot 10^6$ for the OCWT and $Re = 1.6 \cdot 10^6$ for the CCWT, with $D_t$ equal to 1.96 m and 1.85 m, respectively. This suggests that the tunnels are mechanically similar, and the comparison between scaled quantities can be performed even if the reference velocities are different.

### B. Methods and results

Two pairs of cross sections have been selected to perform the comparison. For the inlet region, we will refer to sections S1 ($x/H = 0.06$) and S1b ($x/H = 0.33$) belonging to IISTA and CET tunnel, respectively. For the test region, we will refer to section S5 ($x/H = 6.06$) and section S2b ($x/H = 5.26$). Data are available at


Published under license by AIP Publishing

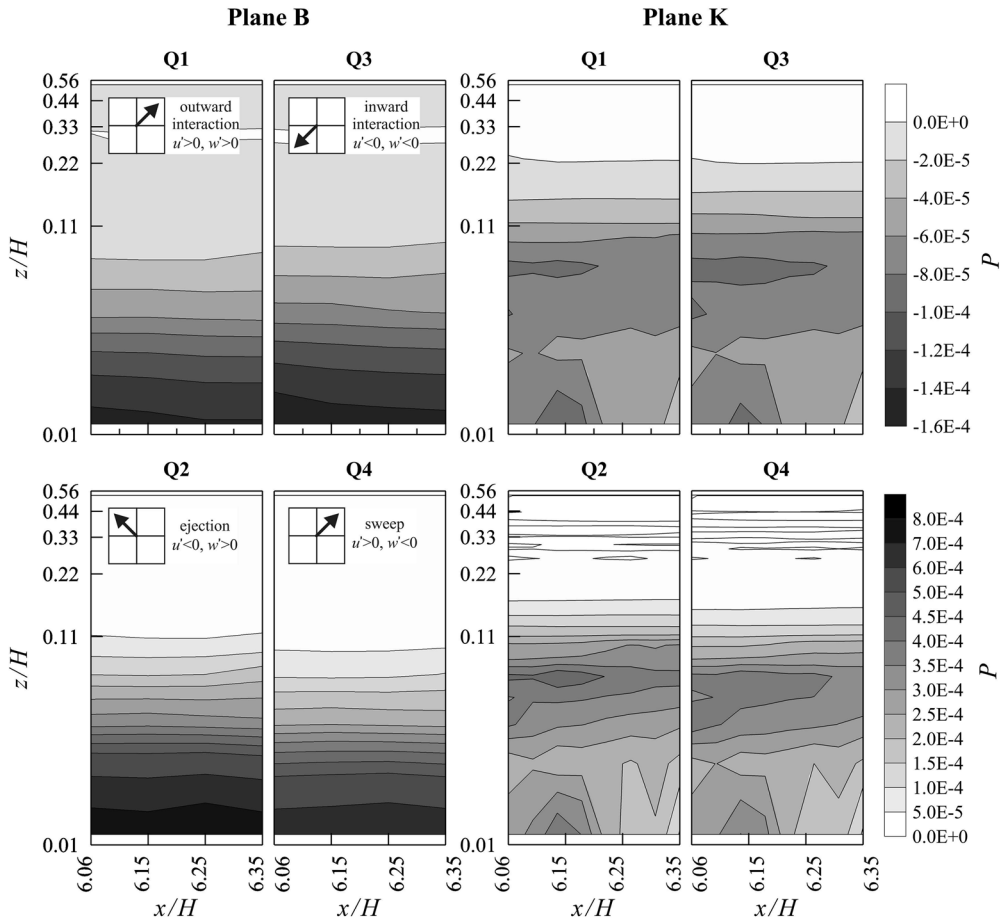


**FIG. 16**. Time-averaged production of the turbulent kinetic energy by the Reynolds shear stress of each quadrant decomposed.

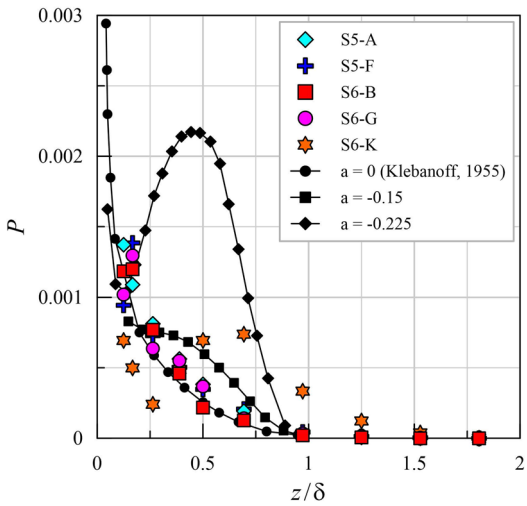


**FIG. 17**. Mean turbulent energy production for some vertical profiles in the test region.

nine points within the area where models are usually located and measurements are taken. The points are in the lower-central area of the section, avoiding (i) excessive proximity to the walls, (ii) possible distortions due to the different width of the tunnels, and (iii) the blockage effect exerted by the lateral and upper contours of the section [see Fig. 18(b)]. The coordinates of the points are measured in a coordinate system with origin on the bottom at the center of the section (Tables III and IV report the coordinates in millimeters).

The comparison concerns the non-dimensional mean velocity, $Uc = u/u_{\mathrm{ref}}$, and the turbulent intensity, $ITc$ (%). Table III contains the values measured at the inlet cross section in both the tunnels; Table IV contains the same for the test cross section. A comparison parameter for the turbulence intensity is also reported: $r_I = I_{\mathrm{IISTA}}/I_{\mathrm{CET}}$, which is the ratio between the turbulence intensities in the two tunnels. Values of $r_I$ lower than unity mean that the turbulence intensity is lower in the IISTA tunnel than in the CET tunnel.

The non-dimensional velocity data are represented in Fig. 19. Considering the inlet regions, a comparison can be made between panels (a) and (c). Both the tunnels present (i) a negative gradient


Published under license by AIP Publishing

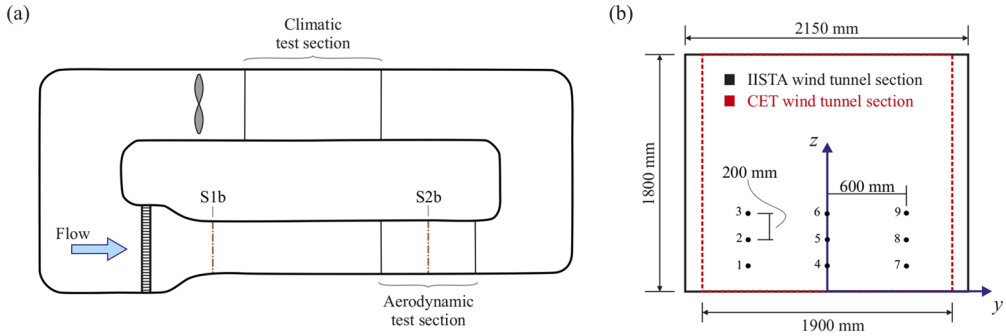


**FIG. 18**. Climatic boundary layer wind tunnel at CET. (a) Layout of the tunnel showing (i) the two test sections (i.e., aerodynamic and climatic), (ii) the turbine, (iii) the mouthpiece, and (iv) the section for the placement of roughness elements. A more complete sketch is shown in the work of Ref. 13. (b) Cross section S2 compared with the section of the IISTA wind tunnel (OCWT is represented in black and CCWT in red). The points selected for the comparison are shown (1–9).

from the left-hand side to the right-hand side and (ii) velocities slightly lower with respect to the reference one. In the case of the CET tunnel, the gradient can be expression of the flow field non-homogeneity induced by the curves of the closed circuit. In the case of the IISTA tunnel, it is probably due to the lack of symmetry in the positioning of the tunnel in the hosting room. Panels (b) and (d) allow the comparison of the velocity distribution in the test regions. The flow is more homogeneous in the IISTA tunnel with respect to the CET one, with values very closed to the reference velocity and minimal gradients. We infer that the open circuit geometry allows the flow to recover uniformity, while that does not happen in the other facility. Also a quantitative analysis is performed by considering the local flow velocity deviation from the average velocity,

$$Dev = \frac{U - \overline{U}}{\overline{U}}, \tag{21}$$

where $U$ is the local velocity and $\overline{U}$ is the average velocity over section. A zero deviation means that the local velocity magnitude is the same as that of average velocity. The average deviation index explains the overall behavior of flow uniformity, and it can be calculated as

$$DI = \left( \int_{A_0} \frac{U - \overline{U}}{\overline{U}} dA \right) A_0^{-1}, \tag{22}$$

where $dA$ is the differential element of area and $A_0$ is the total area of the section. The deviation index represents local distribution very well in cases where the flow uniformity is high.[33] In the IISTA tunnel, $DI$ is equal to 1.7% and 0.8% for the inlet and test section, respectively. In the CET tunnel, the deviation index is higher, with values equal to 2.2% (inlet section) and 1.9% (test section).

The turbulence intensity is generally higher in the IISTA tunnel, with the exception of the lower part of the inlet cross section, where the ratio $r_I$ presents values between 0.8 and 1. The main differences can be found in the test cross section, with values of $r_I$ up to 2.9, especially in the lower region. Figure 20 shows the contour maps of the parameter $r_I$. In any case, the maximum value of the turbulent intensity is equal to 4.3%.

**TABLE III**. Data in the inlet cross sections S1 and S1b (IISTA and CET tunnel, respectively).

| | | | $Uc$ (-) | | $ITc$ (%) | | |
|---|---|---|---|---|---|---|---|
| Point (#) | y (mm) | z (mm) | IISTA | CET | IISTA | CET | $r_I$ |
| 1 | −600 | 200 | 0.96 | 0.91 | 1.4 | 1.8 | 0.8 |
| 2 | −600 | 400 | 0.96 | 0.91 | 1.3 | 1 | 1.3 |
| 3 | −600 | 600 | 0.95 | 0.92 | 1.4 | 1.1 | 1.3 |
| 4 | 0 | 200 | 0.93 | 0.90 | 1.2 | 1.3 | 0.9 |
| 5 | 0 | 400 | 0.93 | 0.91 | 1.2 | 1 | 1.2 |
| 6 | 0 | 600 | 0.93 | 0.90 | 1.4 | 1.2 | 1.2 |
| 7 | 600 | 200 | 0.92 | 0.86 | 1.1 | 1.4 | 0.8 |
| 8 | 600 | 400 | 0.91 | 0.87 | 1.4 | 1.5 | 0.9 |
| 9 | 600 | 600 | 0.90 | 0.86 | 2.4 | 1.8 | 1.3 |
| Mean value | | | 0.93 | 0.89 | 1.42 | 1.34 | 1.08 |
| Standard deviation | | | 0.02 | 0.02 | 0.38 | 0.31 | 0.22 |

**TABLE IV**. Data in the test cross sections S5 and S2b (IISTA and CET tunnel, respectively).

| | | | $Uc$ (-) | | $ITc$ (%) | | |
|---|---|---|---|---|---|---|---|
| Point (#) | y (mm) | z (mm) | IISTA | CET | IISTA | CET | $r_I$ |
| 1 | −600 | 200 | 0.98 | 0.99 | 3.0 | 2.5 | 1.2 |
| 2 | −600 | 400 | 0.98 | 1.01 | 1.3 | 1.3 | 1.0 |
| 3 | −600 | 600 | 0.97 | 1.02 | 1.5 | 1.0 | 1.5 |
| 4 | 0 | 200 | 0.99 | 0.99 | 4.3 | 1.5 | 2.9 |
| 5 | 0 | 400 | 1.00 | 0.99 | 1.9 | 1.2 | 1.6 |
| 6 | 0 | 600 | 1.00 | 0.98 | 1.8 | 0.9 | 2.0 |
| 7 | 600 | 200 | 0.99 | 0.96 | 3.2 | 1.5 | 2.1 |
| 8 | 600 | 400 | 1.00 | 0.96 | 1.6 | 1.4 | 1.1 |
| 9 | 600 | 600 | 0.99 | 0.95 | 2.4 | 1.8 | 1.3 |
| Mean value | | | 0.99 | 0.98 | 2.09 | 1.54 | 1.64 |
| Standard deviation | | | 0.01 | 0.02 | 0.83 | 0.46 | 0.60 |


Published under license by AIP Publishing

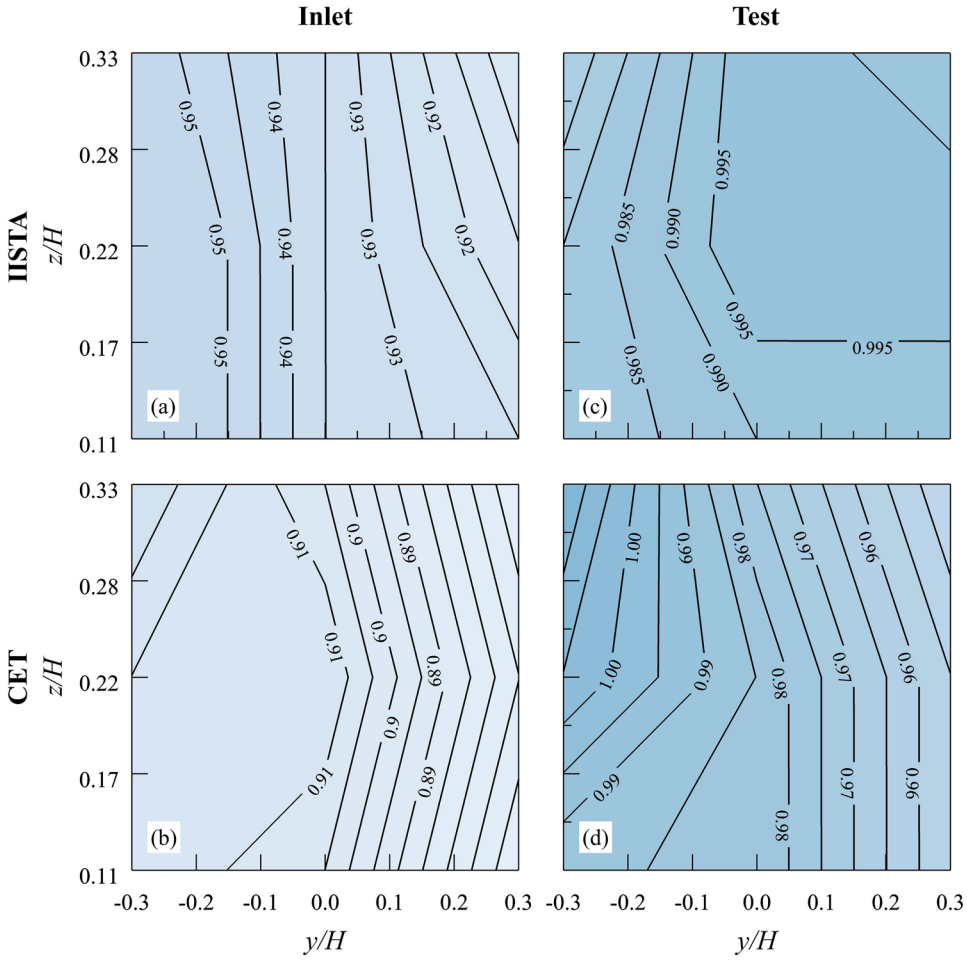


**FIG. 19**. Non-dimensional wind velocity, $u/U_{ref}$. Panel (a) and panel (b) refer to the IISTA inlet and test region, respectively. Panel (c) and panel (d) refer to the CET inlet and test region, respectively.

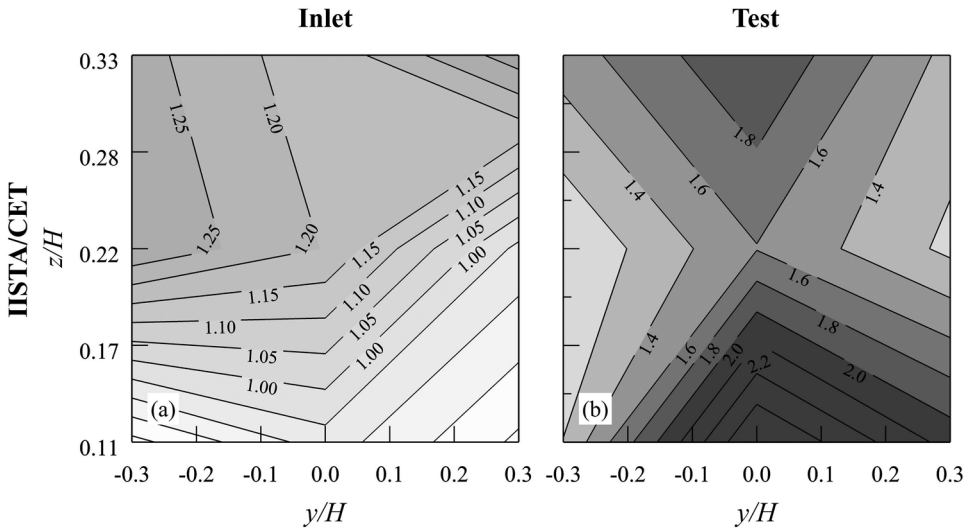


**FIG. 20**. Ratio of the turbulent intensity in the OCWT tunnel with respect to the same quantity in the CCWT tunnel.


Published under license by AIP Publishing

## V. CONCLUSIONS

The multidisciplinary use of wind tunnels and its application to different systems and work scales makes it necessary to guarantee the correct functioning of the facility and to carry out a continuous monitoring.

Experimental tests to study the air flow inside a boundary layer wind tunnel have been carried out in the open-circuit wind tunnel of the Andalusian Institute for Earth System Research from the University of Granada (Spain). The analysis regards the mean and turbulent characteristics of the flow, it includes details about the turbulence production, the Reynolds stress, the vertical velocity skewness, the vorticity, and the spectral properties, and finally, a quadrant decomposition was conducted too. To get an overview of the tunnel performance, data have been taken for the tunnel entrance and the test section.

For both sections, there are a flow retardation and turbulence enhancement in areas adjacent to the wall; however, at a distance large enough from the side walls, the wind field is quite homogeneous. Agreement between the power spectra of the streamwise velocities and the von Karman spectrum is very good in and out of the boundary layer, except for the highest frequencies. For both sections, the curl angular velocity is almost nil out of the boundary layer but increases toward the bottom, being higher for the entrance of the tunnel, with a clockwise rotation direction.

A detailed description of the turbulence structure is provided by the quadrant analysis, where Reynolds stresses contributions are categorized according to their sign. In the boundary layer, (i) ejections and sweeps are the main contributors to the transfer of momentum, (ii) the energy transfer is confined to the boundary layer and reaches a maximum near the surface, and (iii) the turbulence intensity has increasing values toward the bottom. To complete the turbulence analysis, according to the results for the vertical velocity skewness, it has been proven that there is a turbulent kinetic energy transport upwards.

A lack of symmetry in the behavior of the tunnel has been observed. This behavior could be addressed to the positioning of the tunnel in the hosting room, with an external recirculation of the air that cannot be symmetrical.

The results obtained for the OCWT have been compared with similar data from the climatic boundary layer wind tunnel from the Center of Excellence Telč (Czech Republic), a closed-circuit wind tunnel. This comparison shows that, in both tunnels, velocities are slower with respect to the reference one. The mean flow is more homogeneous in the OCWT, but the turbulence intensity is generally higher. Finally, similar values of the Reynolds number suggest that the tunnels are mechanically similar.

In summary, we have performed a flow characterization that (i) allows us to estimate the behavior of an open circuit wind tunnel and (ii) represents a fundamental knowledge to better schedule tests and to better interpret results of future activity. Moreover, this work is a collection of useful data for the improvement of similar CCWTs or for the design of new devices.

Based on the results obtained, a series of modifications are proposed, which may be applicable to all tunnels under similar conditions. For example, the open circuit tunnel should be isolated from the hosting room conditions by eliminating all possible elements that, being located in the room, could generate distortions. This should result in an improvement of the air flow generated in the exterior circuit around the tunnel. A first enhancement can be achieved by installing some deflectors in the room, especially in the area close to the turbine, in order to adjust the symmetry of the flow. Unfortunately, in the present case, it is not possible to install control sections (e.g., critical flow Venturi and sonic throat) that are widely used to improve the behavior of similar devices. This limitation is common to all the cases with a lack of space around the tunnel and a limited length of the tunnel itself. Furthermore, the turbulent intensity could be reduced by (i) improving the flow conditioner (honeycomb) at the entrance, placing screens in the settling duct,[34] and (ii) modifying the roughness of the surfaces where the turbulence is generated (e.g., replacing the tunnel panels with new sheets of a smoother material). Some imperfections (small steps and gaps) can be present at the joints between the panels, they may be due to the deformation of the structure, and they should be removed to obtain a better behavior of the facility.

## NOMENCLATURE

| | |
|---|---|
| $ABL$ | atmospheric boundary layer |
| $C$ | constant for smooth-walled flows |
| $CAV$ | curl angular velocity |
| $CCWT$ | closed circuit wind tunnel |
| $CET$ | Center of Excellence Telč |
| $CFD$ | computational fluid dynamics |
| $Dev$ | local flow velocity deviation |
| $DI$ | deviation index |
| $D_t$ | hydraulic diameter |
| $FFT$ | fast Fourier transform |
| $HWA$ | hot wire anemometer |
| $IT$ | turbulence intensity |
| $IISTA$ | Andalusian Institute for Earth System Research |
| $ITAM$ | Institute of Theoretical and Applied Mechanics |
| $ITc$ | turbulence intensity comparison |
| $k$ | von Karman constant |
| $L_u$ | longitudinal length scale |
| $n$ | frequency |
| $Ni$ | number of events |
| $OCWT$ | open circuit wind tunnel |
| $P$ | production term |
| $Re$ | Reynolds number |
| $Re_x$ | Reynolds number in the x direction |
| $r_I$ | ratio between the turbulence intensities |
| $s$ | skewness |
| $t$ | time |
| $TKE$ | turbulent kinetic energy |
| $U$ | longitudinal wind velocity |
| $u$ | wind velocity |
| $Uc$ | mean velocity comparison |
| $u'$ | gust velocity |
| $u_*$ | friction velocity |
| $u_*^2$ | kinematic momentum flux |
| $\overline{u'v'}$ | shear stress |
| $WTW$ | wind tunnel width |
| $x$ | distance from the beginning of the inlet region |
| $z$ | height |
| $z_b$ | thickness of the boundary layer |


Published under license by AIP Publishing

| | |
|---|---|
| $z_o$ | aerodynamic roughness length |
| $\delta$ | boundary layer thickness |
| $\mu$ | air dynamic viscosity |
| $\rho$ | air density |
| $\sigma^2$ | variance |
| $\tau$ | stress |

## DATA AVAILABILITY

The data that support the findings of this study are available from the corresponding author upon reasonable request.

## REFERENCES


[1] E. Simiu and D. Yeo, *Wind Effects on Structures: Modern Structural Design for Wind* (John Wiley & Sons, 2019).

[2] N. Coudou, S. Buckingham, and J. van Beeck, "Experimental study on the wind-turbine wake meandering inside a scale model wind farm placed in an atmospheric-boundary-layer wind tunnel," J. Phys.: Conf. Ser. **854**, 012008 (2017).

[3] C. Gromke, "Wind tunnel model of the forest and its Reynolds number sensitivity," J. Wind Eng. Ind. Aerodyn. **175**, 53–64 (2018).

[4] Y. Hao, G. A. Kopp, C.-H. Wu, and S. Gillmeier, "A wind tunnel study of the aerodynamic characteristics of a scaled, aeroelastic, model tree," J. Wind Eng. Ind. Aerodyn. **197**, 104088 (2020).

[5] J. B. Barlow, W. H. Rae, and A. Pope, *Low-Speed Wind Tunnel Testing* (John Wiley & Sons, 1999).

[6] K. Varshney and K. Poddar, "Experiments on integral length scale control in atmospheric boundary layer wind tunnel," Theor. Appl. Climatol. **106**, 127–137 (2011).

[7] J. M. L. Mattuella, A. Loredo-Souza, M. G. K. Oliveira, and A. P. Petry, "Wind tunnel experimental analysis of a complex terrain micrositing," Renewable Sustainable Energy Rev. **54**, 110–119 (2016).

[8] I. D. Azzawi and A. F. Hasan, "Comparison and optimization design methodology for open-loop subsonic wind tunnel," in *2018 1st International Scientific Conference of Engineering Sciences—3rd Scientific Conference of Engineering Science (ISCES)* (IEEE, 2018), pp. 186–191.

[9] X. X. Cheng, J. Dong, Y. Peng, L. Zhao, and Y. J. Ge, "Full-scale/model test comparisons to validate the traditional ABL wind tunnel simulation technique: A literature review," Preprint **2017**, 2017100046.

[10] A. M. Aly and H. Gol-Zaroudi, "Atmospheric boundary layer simulation in a new open-jet facility at LSU: CFD and experimental investigations," Meas.: J. Int. Meas. Confed. **110**, 121–133 (2017).

[11] A. Abdel-Rahman, M. Agelin-Chaab, G. Elfstrom, and J. Komar, "Integrated aero-thermal testing of a race car in a full scale climatic wind tunnel," Technical Report 2016-01-1588, https://doi.org/10.4271/2016-01-1588 SAE Technical Paper, 2016.

[12] M. Ainegren, S. Tuplin, P. Carlsson, and P. Render, "Design and development of a climatic wind tunnel for physiological sports experimentation," Proc. Inst. Mech. Eng., Part P **233**, 86–100 (2019).

[13] S. Kuznetsov, M. Ribičić, S. Pospíšil, M. Plut, A. Trush, and H. Kozmar, "Flow and turbulence control in a boundary layer wind tunnel using passive hardware devices," Exp. Tech. **41**, 643–661 (2017).

[14] M. Jiménez-Portaz, M. Clavero, and M. Losada, "Experimental analysis of wind interaction with olive grove and the atmospheric surface boundary layer," Eur. J. Sustain. Dev. **8**, 180 (2019).

[15] M. Jiménez-Portaz, F. Bello-Millán, P. Folgueras, M. Clavero, and M. Losada, "Wind flow around a wind turbine system over hilly terrain and its environmental effects: Wind tunnel tests," in ICREPQ, 2016.

[16] P. Rodríguez Folgueras *et al.*, "Caracterización del campo de vientos a sotavento de un aerogenerador marino. Influencia de la inclinación del rotor sobre el afloramiento de aguas profundas," Ph.D dissertation (University of Granada, 2012). Retrieved from: http://hdl.handle.net/10481/32327 (2012).

[17] J. A. Cuesta Cañas *et al.*, "Comportamiento aerodinámico de un dispositivo ahuyenta aves y estudio de campos de viento sobre topografía compleja," Ph.D. dissertation (University of Granada, 2008). Retrieved from: http://hdl.handle.net/10481/2116 (2008).

[18] T. Theodorsen, "Mechanisms of turbulence," in *Proceedings of the Second Midwestern Conference on Fluid Mechanics* (Ohio State University, Colombus, OH, 1952), p. 1952.

[19] H. Schlichting and K. Gersten, *Boundary-Layer Theory* (Springer, 2016).

[20] L. P. Chamorro, R. Arndt, and F. Sotiropoulos, "Reynolds number dependence of turbulence statistics in the wake of wind turbines," Wind Energy **15**, 733–742 (2012).

[21] R. Stull, *Practical Meteorology: An Algebra Based Survey of Atmospheric Science* (BC Campus, 2016), p. 12.

[22] V. Uruba, *Turbulence Handbook for Experimental Fluid Mechanics Professionals* (OPTEK, 2012).

[23] F. T. Nieuwstadt, J. Westerweel, and B. J. Boersma, *Turbulence: Introduction to Theory and Applications of Turbulent Flows* (Springer, 2016).

[24] X. Xie, L. Cao, and H. Huang, "Thickened boundary layer theory for air film drag reduction on a van body surface," AIP Adv. **8**, 055129 (2018).

[25] H. Kozmar and B. Laschka, "Wind-tunnel modeling of wind loads on structures using truncated vortex generators," J. Fluids Struct. **87**, 334–353 (2019).

[26] Y. Tian, Q. Yang, N. Yang, B. Li, and B. Chen, "Statistical spectrum model of wind velocity at Beijing meteorological tower," Sci. China: Technol. Sci. **54**, 2869 (2011).

[27] J. Carlier and M. Stanislas, "Experimental study of eddy structures in a turbulent boundary layer using particle image velocimetry," J. Fluid Mech. **535**, 143 (2005).

[28] K. Takahashi, "Incorporating a tensor in the effective viscosity model of turbulence and the Reynolds stress," AIMS Math. **3**, 554 (2018).

[29] F. Champagne, V. Harris, and S. Corrsin, "Experiments on nearly homogeneous turbulent shear flow," J. Fluid Mech. **41**, 81–139 (1970).

[30] R. J. Hogan, A. L. Grant, A. J. Illingworth, G. N. Pearson, and E. J. O'Connor, "Vertical velocity variance and skewness in clear and cloud-topped boundary layers as revealed by Doppler lidar," Q. J. R. Meteorol. Soc. **135**, 635–643 (2009).

[31] S. Longo and M. A. Losada, "Turbulent structure of air flow over wind-induced gravity waves," Exp. Fluids **53**, 369–390 (2012).

[32] K. Nolan, E. Walsh, and D. McEligot, "Quadrant analysis of a transitional boundary layer subject to free-stream turbulence," J. Fluid Mech. **658**, 310 (2010).

[33] C. Om Ariara Guhan, G. Arthanareeswaran, K. Varadarajan, and S. Krishnan, "Numerical optimization of flow uniformity inside an under body-oval substrate to improve emissions of IC engines," J. Comput. Des. Eng. **3**, 198–214 (2016).

[34] L. Cattafesta, C. Bahr, and J. Mathew, "Fundamentals of wind-tunnel design," in *Encyclopedia of Aerospace Engineering*, edited by R. Blockley and W. Shyy (Wiley, 2010).



Published under license by AIP Publishing